


Geophysical Research Letters®

RESEARCH LETTER

10.1029/2024GL110852

Thermochemistry of the Mantle Transition Zone Beneath the Western Pacific

Lauren Waszek¹ , Rashni Anandawansha², Justin Sexton^{1,3}, and Benoit Tauzin^{4,5} 

¹James Cook University, Douglas, QLD, Australia, ²New Mexico State University, Las Cruces, NM, USA,

³Commonwealth Scientific and Industrial Research Organisation, Douglas, QLD, Australia, ⁴ENS Lyon, Lyon, France,

⁵Australian National University, Acton, ACT, Australia

Key Points:

- New data sets of ScSScS precursors beneath the western Pacific subduction zones are compiled and analyzed with machine learning methods
- High-resolution measurements of transition zone discontinuities and mineralogical modeling provide detailed maps of thermochemistry
- Thermochemical models track recent mantle circulation patterns, indicating slab stagnation, basalt accumulation, and interaction with plumes

Supporting Information:

Supporting Information may be found in the online version of this article.

Correspondence to:

L. Waszek,
lauren.waszek@cantab.net

Citation:

Waszek, L., Anandawansha, R., Sexton, J., & Tauzin, B. (2024). Thermochemistry of the mantle transition zone beneath the western Pacific. *Geophysical Research Letters*, 51, e2024GL110852. <https://doi.org/10.1029/2024GL110852>

Received 24 JUN 2024

Accepted 12 SEP 2024

Author Contributions:

Conceptualization: Lauren Waszek

Formal analysis: Lauren Waszek, Justin Sexton

Funding acquisition: Lauren Waszek

Investigation: Lauren Waszek, Rashni Anandawansha

Methodology: Lauren Waszek, Rashni Anandawansha, Justin Sexton, Benoit Tauzin

Project administration: Lauren Waszek

Software: Lauren Waszek, Justin Sexton, Benoit Tauzin

Supervision: Lauren Waszek

Visualization: Lauren Waszek, Rashni Anandawansha, Justin Sexton

Writing – original draft: Lauren Waszek

Abstract The Earth's mantle transition zone has significant control on material flux between upper and lower mantle, thus constraining its properties is imperative to understand dynamic processes and circulation patterns. Global seismic data sets to study the transition zone typically display highly uneven spatial distribution. Therefore, complementary geometries are essential to improve knowledge of physical structures, thermochemistry, and impact on convection. Here, we present a new automated approach utilizing machine learning to analyze large seismic data sets, and derive high-resolution maps of transition zone discontinuity properties. Seismic measurements from ScSScS precursors are integrated with mineralogical modeling to constrain thermochemistry of the western Pacific subduction zone. Our models map recent subduction patterns through the transition zone, indicating stagnation of slabs and accumulation of basalt at its base, and interaction between stagnant slabs and plumes. These results suggest that the thermochemical properties of upper mantle discontinuities can provide high-resolution images of mantle circulation patterns.

Plain Language Summary Earth's upper mantle displays several discontinuous jumps in its physical properties, which result from changes in its mineral structure as pressure and temperature increase with depth. The major transitions near to 410 and 660 km depth are associated with physical changes that have significant influence on the flow of hot upwelling plumes and cold downgoing slabs. The depth and strength of the discontinuities depend on the local temperature and composition, and therefore constraining these properties can help to track mantle circulation patterns and better understand convection behavior. Global seismic data sets are highly uneven in spatial coverage, and therefore must be supplemented by data sets with different spatial sensitivity. Here, we present an automated approach based on machine learning to analyze seismic phases with such complementary geometry, and apply these techniques to investigate subduction zones beneath the western Pacific. We incorporate high-resolution observations of the discontinuities with modeling from mineral physics, producing new models of temperature and composition in this region. The models track recent convection patterns through the transition zone, indicating ponding of slabs and plumes. These results suggest that the temperature and composition of the transition zone can be used to provide detailed maps of mantle circulation.

1. Introduction

The upper mantle comprises several mineralogical phase transformations, variously caused by changes in pressure, temperature, and composition. These phase changes create discontinuous jumps in density and seismic velocity that may be detected by reflected and converted seismic waves. Two major global discontinuities at 410 and 660-km depth demarcate the mantle transition zone (MTZ), a layer of particular structural and rheological complexity which separates the upper and lower mantle, and modulates heat flux and rock flow. The “410” and “660” result from transitions from olivine to wadsleyite, and ringwoodite to bridgmanite and ferropericlase respectively (Christensen, 1995). Their physical properties are linked to ambient thermochemistry (Stixrude & Lithgow-Bertelloni, 2011), whereby their depth separation is a thermometer for the upper mantle (Houser & Williams, 2009; Ritsema et al., 2009; Shearer & Flanagan, 1999), and impedance contrast relates to composition (Munch et al., 2020; Tauzin et al., 2022; Yu et al., 2023).

The MTZ discontinuities have significant influence on global mantle circulation, particularly the 660. Its endothermic ringwoodite decomposition and associated viscosity increase is expected to impede convecting material (Fukao & Obayashi, 2013; Tackley et al., 1993). Seismically, velocity tomography models show that both hot upwelling plumes and cold downgoing slabs become deflected near to the base of the MTZ (French

© 2024. The Author(s).

This is an open access article under the terms of the [Creative Commons Attribution License](https://creativecommons.org/licenses/by/4.0/), which permits use, distribution and reproduction in any medium, provided the original work is properly cited.

Writing – review & editing:Lauren Waszek, Rashni Anandawansha,
Justin Sexton, Benoit Tauzin

& Romanowicz, 2014; Fukao & Obayashi, 2013; Ritsema et al., 2011). The phase decomposition of garnet dominates at high temperatures; this exothermic reaction is predicted to promote efficient upward transportation of hot material (Hirose, 2002). This reaction is accessed only at very high temperatures, in regions which are mostly too small to be resolved by long period seismic data sets typically used for global studies of the MTZ (Waszek et al., 2021). Similarly, the small cold regions associated with stagnant slabs also require higher resolution regional studies. Improved constraints on these features is necessary to better understand compositional layering and basaltic enrichment processes associated with stagnation at the MTZ.

The major seismic phases to study the MTZ on a global scale are precursors to SS and PP (Deuss, 2009; Houser & Williams, 2009; Huang et al., 2019; Schmerr & Garnero, 2007; Shearer & Flanagan, 1999; Waszek et al., 2021; Yu et al., 2023), and receiver functions (Lawrence & Shearer, 2006; Munch et al., 2020; Pugh et al., 2021; Tauzin et al., 2008; Vinnik, 1977). However, inhomogeneous data distribution results in significant variability in spatial resolution, with particularly sparse coverage in the southern hemisphere. Thus, incorporating various seismic data is essential to improve resolution on a global scale (Yu et al., 2023). Here, we explore the potential of using various automated approaches to constrain MTZ structures, applied as proof-of-concept to ScSScS precursors. ScSScS precursors are part of the ScS reverberation family of seismic phases (Courtier & Revenaugh, 2007; Haugland et al., 2019; Revenaugh & Jordan, 1991; Shearer, 1991; Wang et al., 2017), and provide a contrasting geometry to other phases (Figure 1).

We select the western Pacific region due to its poor coverage by SS and PP data, yet relatively high coverage for ScS reverberations (Courtier & Revenaugh, 2007; Suetsugu et al., 2004) (Figure 1 and Figure S1 in Supporting Information S1). This region has diverse dynamical features associated with its subduction zones. The downgoing slabs bounding the western edge of the Pacific display a variety of regimes and stages of subduction and stagnation (Fukao & Obayashi, 2013), and complex interactions between the Tonga-Kermadec slab and Samoan plume (Chang et al., 2016), as well as the Caroline hotspot with the Pacific slab (Obayashi et al., 2021). Improved constraints on these regions may help to better understand the mechanisms which determine the extent of slab stagnation (Fukao & Obayashi, 2013; Waszek et al., 2018), and correlation to the large earthquakes associated with slab subduction (Conrad et al., 2004).

Our study combines procedures to automatically process data from raw seismograms to thermochemical maps, integrating seismology with mineral physics (Garcia et al., 2021a; Tauzin et al., 2022; Waszek et al., 2021). We use “Autopicker” (Garcia et al., 2021a), a machine learning picking algorithm, to rapidly and consistently compile a large regional data set beneath the western Pacific, which we compare with a handpicked data set. We implement adaptive stacking (AS) (Waszek et al., 2021) to obtain measurements of the MTZ discontinuities with laterally variable resolution. Incorporating mineralogy from upper mantle thermochemical models, we use Bayesian inversion techniques to generate new thermochemical maps of the MTZ. Clustering analysis is employed to obtain measurements of upper mantle discontinuities from individual seismograms, extracting signals undetectable by the human eye. Our new thermochemical models track convection patterns in the MTZ, mapping slab subduction through the 410 and stagnation at 660. The models also indicate ponding of upwelling material beneath the MTZ, with interaction between the Samoan and Caroline plumes and stagnant slabs.

2. Data Processing and Compilation

ScSScS is a shear wave phase which reflects twice from the core-mantle boundary, and once at Earth's surface (Figure 1). Precursors to ScSScS are generated by underside reflections from mantle discontinuities at the midpoint. Their short epicentral distances (0–60°) produce a complementary geometry to other seismic phases used for mantle measurements, such as SS and PP, which are typically studied at much larger distances, and the near-vertical reflection provides sensitivity to small-amplitude discontinuity variations.

We downloaded data from SAGE for events from 1 January 1990 to 31 December 2020. All processing uses the Seismic Analysis Code (Goldstein et al., 2003). Our event criteria is magnitude $M_w \geq 6$, source depth greater than 80 km, and epicentral distances less than 60° (Courtier & Revenaugh, 2007; Haugland et al., 2019). To focus on the western Pacific region, we select events with longitude 90–190° and latitude –60–40°, and seismograms with bounce points within longitude 90–200° and latitude below 60° (Figure 1 and Figure S1 in Supporting Information S1). The data were rotated to the transverse component, then bandpass filtered between 15–100 s. We discarded data with a signal-to-noise ratio lower than 2, where noise is the root-mean-square amplitude in the window –400 to –50 s before the theoretical ScSScS arrival, and signal is the maximum peak displacement

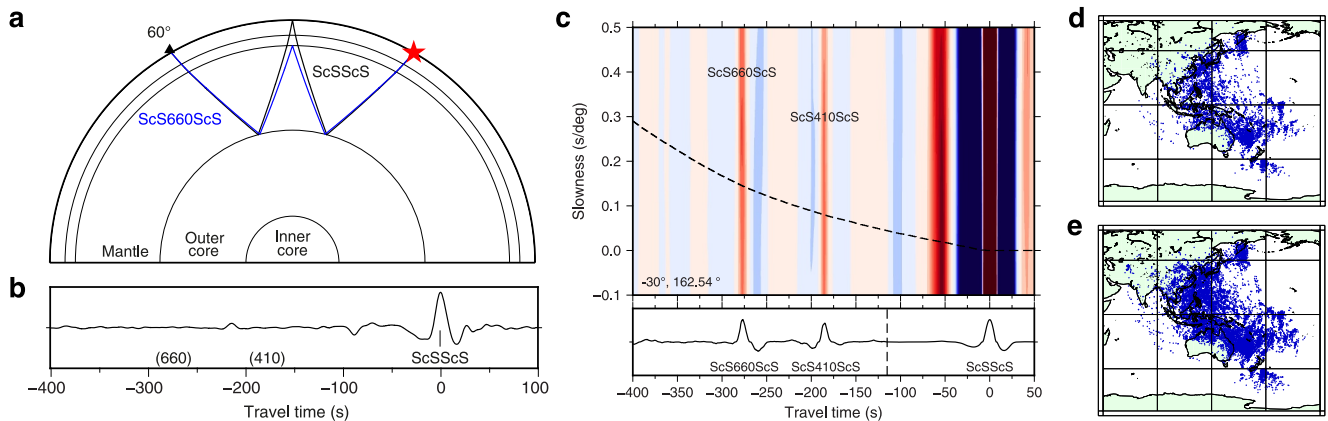


Figure 1. ScSScS data. (a) Ray paths of ScSScS and ScS660ScS. (b) Example of individual seismogram in displacement, from station POHA, event in Fiji on 9 November 2022. (c) Example of second root vespigram showing clear 410 and 660 signals. Colors represent arrival energy (red is positive, blue is negative), and this is normalized to the ScSScS amplitude. The dashed line is the theoretical time and slowness of ScSScS precursors relative to the main phase, as calculated from PREM. The cross-section beneath the vespigram is taken along this line. The precursor window has magnification of 63.5 relative to the ScSScS window; the ScS660ScS amplitude is 1.57% of the ScSScS. (d) Handpicked data bounce points. (e) Automatically picked data bounce points.

within ± 50 s of the theoretical arrival, as calculated from PREM (Dziewoński & Anderson, 1981) using the TauP Toolkit (Crotwell et al., 1999). This resulted in 32,960 seismograms prior to picking.

We compiled both handpicked and automatically picked (“autopicked”) data sets. “Picking” involves identifying the ScSScS signal on a seismogram guided by the theoretical arrival time, then picking and aligning on the maximum peak time. Handpicked data undergo visual quality inspection, examining the waveform consistency, and the data set totals 8,472. The autopicked data is compiled using Autopicker, a seismic waveform identification code based on Convolutional Neural Networks (CNN) (Garcia et al., 2021a). Autopicker uses CNN models trained on seismic phases to identify the best-matching peak in a seismogram within a user-specified time window; we use 40 s. The window iterates along the seismogram for a user-selected time range, outputting the time and quality for the best peak in each window. Quality is the ratio of time windows in which the peak is selected to that in which it is present, and polarity is identified by repeating for the inverse seismogram.

The CNN model was trained on a large handpicked global data set of SS phases (Waszek et al., 2018), which can identify successfully other shear phases with similar frequency content (Garcia et al., 2021a). We search ± 50 s around the theoretical ScSScS time, and retain data with minimum quality of 60%, totaling 18,829. Example seismograms are presented in Figures S2–S4 in Supporting Information S1, selected for high signal-to-noise ratio, to show clearly the ScSScS waveform shapes.

Following picking, the data were aligned to the ScSScS peak maxima and normalized. The data were then corrected for 3D crustal and mantle structure using Crust2.0 (Bassin et al., 2000) and S40RTS (Ritsema et al., 2011), with a background model of PREM (Dziewoński & Anderson, 1981). Following the methodology of Waszek et al. (2021), we calculated a delay time correction for every time point on the seismograms, and hence corrected for all discontinuity depths simultaneously. We further used Autopicker to scan for precursor in individual seismograms (Section 3.2).

3. Seismic Observations of the MTZ

3.1. Stacked Measurements

We stack the seismograms by common reflection point, to suppress noise, and magnify the small precursor signals. We use two approaches for spatial partitioning: evenly distributed regional bins, and adaptive parameterizations (Waszek et al., 2021). We use second root stacking to identify the precursors, measure their depths, and create the AS parameterizations. Since second root stacking distorts waveform shapes, linear stacking is used for amplitude measurements, although this also experiences distortion from incoherent stacking due to 3D heterogeneities, which reduces the measured amplitudes. Prior to stacking, all data are weighted by signal-to-noise ratio

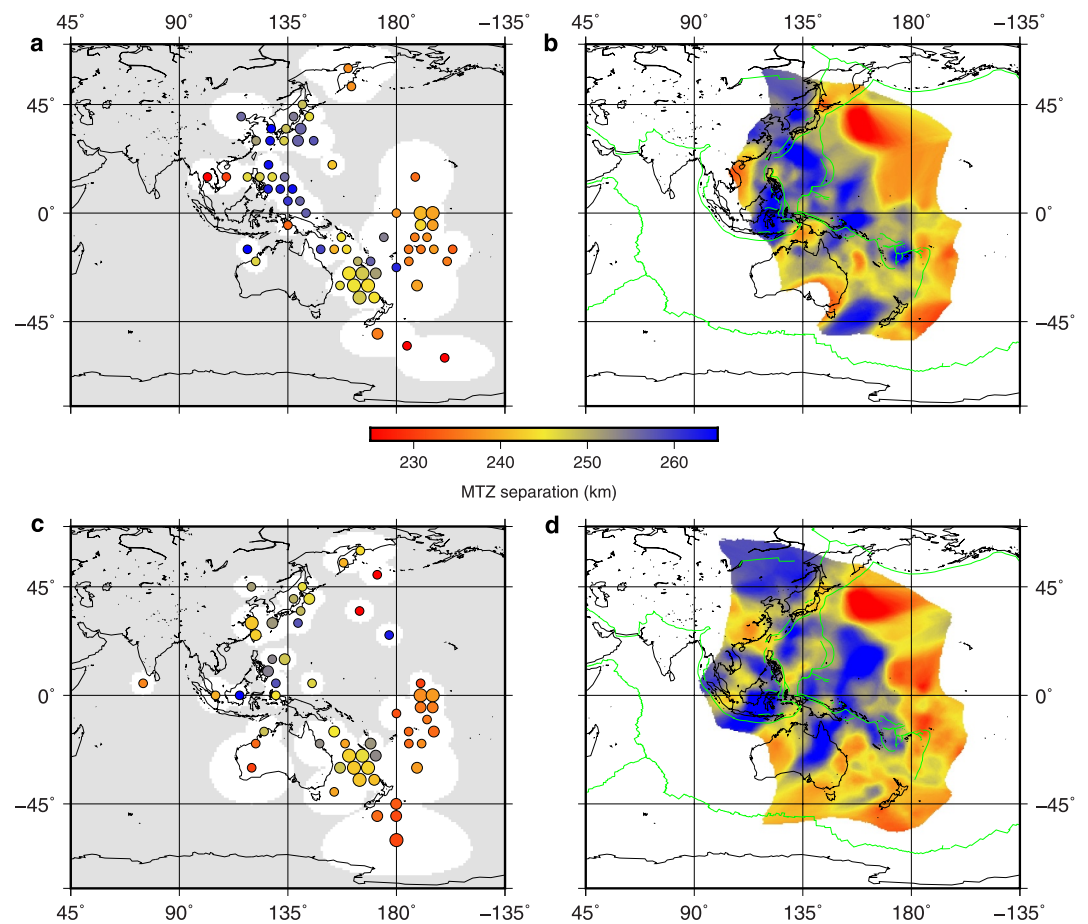


Figure 2. Mantle transition zone thickness observations from stacked ScSScS precursors. (a) Fixed bins, iteratively populated from smallest to largest, handpicked. (b) Adaptive stacking (AS), handpicked. (c) Fixed bins, iteratively populated from smallest to largest, autopicked. (d) AS, autopicked. Complete discontinuity maps of all depths, amplitudes, and errors are contained in the Supplementary Information.

using the root-mean-square amplitude in the depth window 200–800 km (approximately 92–320 s before ScSScS).

We confirm the detectability of the MTZ discontinuities in slant-stacked vespagrams and epicentral distance move-out stacks (e.g., Figure 1 and Figures S5–S10 in Supporting Information S1), corroborated by synthetics (Figures S6–S10 in Supporting Information S1), which confirm there are no predicted interfering phases (Figures S6 and S7 in Supporting Information S1). Regional vespagrams are generated by partitioning the data by reflection point and stacking for overlapping bins of radius 5°, 7.5°, 10°, and 15° (Figure 1). Theoretical precursor arrival times and slownesses are calculated for each bin (Figure 1c and Figures S8–S10 in Supporting Information S1, dashed lines), and amplitudes extracted along these lines to obtain cross-section waveforms. We evaluate the vespagrams for quality, using precursor visibility, waveform shape, noise, and interfering signals, to classify as “a”, “b”, or “c” (see Figures S8–S10 in Supporting Information S1 for examples and descriptions). We measure relative travel time and amplitudes of the 410 and 660 precursors with respect to ScSScS via cross-correlation of the cross-section waveform, and convert times to depths using PREM.

Maps are populated iteratively from smallest to largest bin size (Figures 2a and 2c and Figures S11–S16 in Supporting Information S1), and confirm the visibility of the MTZ discontinuity signals in ScSScS precursor data. The 410 and 660 are detectable in all areas of data coverage, albeit requiring larger bin sizes for regions with fewer data. Overall, the vespagrams are typically noisier and hence poorer quality than either SS or PP (e.g., Deuss (2009); Waszek et al. (2021)), thus justifying the use of second root stack to identify the signals (Figures S8–S10 in Supporting Information S1). The spatial coverage of the retained measurements is similar in quantity,

however with quite different geometries, particularly for the 5° bins. Areas of overlapping geometry show visually good agreement for discontinuity depths, particularly beneath the southern Pacific Ocean, the Tasman and Coral Seas, and Japan.

We next produced smoothed discontinuity maps using AS (Waszek et al., 2021) (Figures 2b and 2d and Figures S17, S18 in Supporting Information S1). The seismograms were first converted from time to depth using PREM. AS generates 2000 randomly located Voronoi nuclei to create a parameterization of stacking cells. After stacking, the maximum amplitude positive peak within ± 30 km of the specified discontinuity is identified, and depth and amplitude measured. Each cell stacks 100 random resamples of the data, producing an average discontinuity depth and amplitude, and standard deviations for error. The cell is removed if the depth error is greater than 15 km, or if no positive peak is detected. The AS procedure iterates until convergence to obtain a global parameterization map, repeating 150 times for smoothed averages.

For each discontinuity, AS obtains lateral maps of the variations in depth and signal amplitude, along with errors. The amplitudes are influenced by event and receiver distributions. We therefore calculate synthetic recreations of the parameterizations for a 1D velocity model (1600 K, 20% basalt), incorporating CMT focal mechanisms (Ekström et al., 2012) and event-receiver geometries. Any amplitude variations result from event-station geometries, and provide amplitude correction factors (Figure S19 in Supporting Information S1). We obtain regional maps of all parameters (Figures 2c and 2d and Figures S20–S23 in Supporting Information S1), via retaining locations with average voronoi cell size less than 10^7 km². We emphasize that the measurements must be analyzed in combination with errors and cell sizes, to determine lateral resolution and error tolerances.

Both handpicked and automatically picked maps produce an average MTZ thickness of 249 km (Table S1 in Supporting Information S1), with some differences in topography. The correlation coefficient of regions of overlapping coverage is 0.6619, attributed to differences in data coverage and parameterizations. The 410 and 660 depths are not correlated for either data set, but are correlated to MTZ thickness as expected (Table S2 in Supporting Information S1). Topography variations must be analyzed in the context of voronoi cell sizes (Figure S18 in Supporting Information S1). Small cells are generated in regions of dense, high quality data, and map lateral variations on the order of 500 km (Figures 2c and 2d and Figures S18, S20–S23 in Supporting Information S1). Larger voronoi cells are found in areas with noisier or fewer data, and their measurements provide a larger spatial average. However, larger cells detect sharp topography changes, since the parameterization process aligns the cell edges to such variability (Figure 2).

Visual inspection reveals good agreement between fixed-bin geometry and AS depth measurements. Comparison to voronoi cell sizes (Figure S18 in Supporting Information S1) highlights the improvement in resolution of AS, which retains greater spatial coverage, and smaller average cell size (Table S3 in Supporting Information S1). This is expected, since fixed-geometry imposes uninformed spatial constraints on the parameterization. Despite varying bin sizes, the predetermined size, shape, and location cannot capture the topography variations, due to averaging. The AS cell shapes adjust for discontinuity topography, and the variable cell size provides information in regions of lower data coverage, albeit with lower lateral resolution (Figure S18 in Supporting Information S1). We consider the AS successful for application to ScSScS, as it identifies precursor signals in stacked data, and produces parameterizations with cell sizes and shapes appropriate to data coverage and discontinuity topography.

Noting differences in resolution, our AS maps show agreement with maps generated from SS precursors (Figures S24a and S24b in Supporting Information S1) (Deuss, 2009; Houser & Williams, 2009; Schmerr & Garnero, 2007; Shearer & Flanagan, 1999; Waszek et al., 2021), displaying thicker MTZ around the edge of the Pacific Ocean and thinner beneath it. They also have good correlation to seismic velocity tomography models within the MTZ (French & Romanowicz, 2014; Ritsema et al., 2011) (Figures S24c and S24d in Supporting Information S1), indicating generally thick (thin) MTZ in regions of high (low) seismic velocity (see Table S2 in Supporting Information S1 for correlation coefficients). The ScSScS measurements provide much higher lateral resolution, and thus map finer scale variations in topography than either SS data or tomography models, evidenced by comparison to voronoi cell size (Figure S18 in Supporting Information S1; Figure S28 in Supporting Information S1 from Waszek et al. (2021)).

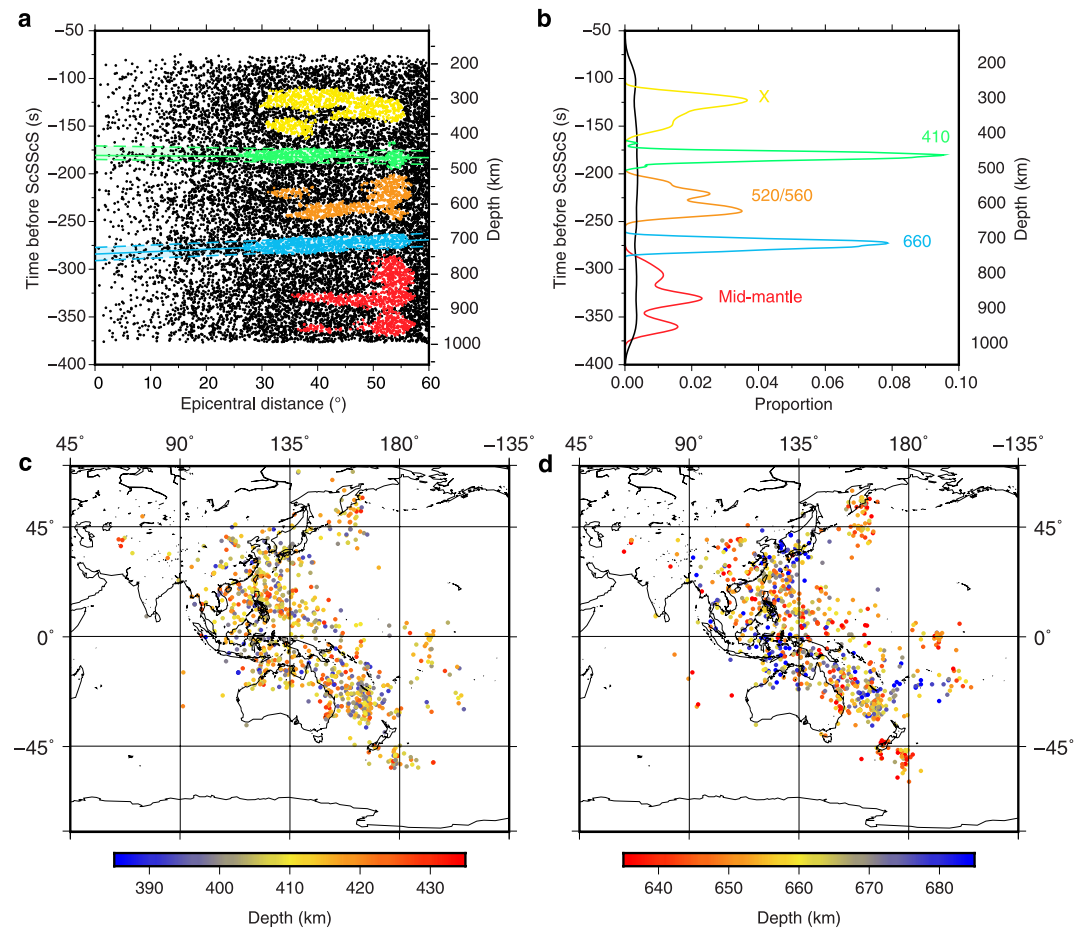


Figure 3. Clustering analysis for autopicked precursors in individual seismograms for the autopicked data set. (a) Clusters identified in epicentral distance moveout in time before ScSScS (depth). Black points correspond to noise, or data that cannot be attributed to the five major depth clusters. Lines correspond to best fit for the 410 and 660, weighted according to pick quality. The 410 arrives earlier than predicted by PREM, and the 660 arrives later; the 660 also displays opposite time-distance relationship. Shaded regions are the unweighted 95% prediction interval. (b) Proportion of points by time before ScSScS (depth), with mantle discontinuity indicated. (c) Depths of picks from the 410 cluster. (d) Depths of picks from the 660 cluster.

3.2. Measurements in Individual Seismograms

Since Autopicker can detect SS precursors in individual seismograms (Garcia et al., 2021a), we investigated its potential for ScSScS precursors. We scanned corrected seismograms from 375–75 s before ScSScS for positive polarity signals, retaining those with quality greater than 60%. This resulted in 15,594 picks for automatically picked data, and 5,127 for handpicked. We performed clustering analysis using the hdbSCAN algorithm (Campello et al., 2013) in the R package “hdbSCAN” (Hahsler et al., 2019), to identify signals potentially associated with discontinuities. This unsupervised machine learning method partitions data into distinctive groups while identifying noise and outliers. Its hierarchical approach identifies clusters across different densities without predefining the number of clusters. We set a minimum number of 200 points, determined by trial and error; both smaller and larger minimum cluster sizes results in amalgamation of clusters from multiple discontinuities.

Using relative time and epicentral distance as inputs, the data sets are partitioned into six clusters, one of which corresponds to noise or data which cannot be attributed clearly to another cluster. The remaining five clusters arrive at times which correspond approximately to the depths of mantle discontinuities (Figure 3 and Figure S25 in Supporting Information S1). The 410 and 660 are clear dominant signals (Figure 3b). The X, 520, and mid-mantle clusters have multimodal depth distributions, with multiple separate patches classified as one cluster,

instead of distinct groups (Figure 3a). This is consistent with dedicated studies of these discontinuities, which detect signals at multiple depths (e.g., Pugh et al. (2021); Tian et al. (2020); Waszek et al. (2018)). Notably, the patches within each cluster display similar time-distance relationships.

The clusters associated with the discontinuities are primarily found at epicentral distances greater than 25–30°. This is due to increasing number of data with epicentral distance, which becomes approximately consistent at 25–30° (Figures S6 and S7 in Supporting Information S1). For the 410 and 660 clusters, we calculate an average line of best fit, weighting the points according to pick quality. We use the unweighted 95% prediction interval to identify points most likely to be associated with reflections from the discontinuities. These differ from PREM, whereby the 410 arrives earlier and the 660 later, as expected for subduction zones.

The spatial distribution of the 410 and 660 clusters reveals much more spatial variability in depth measurements than stacked data (Figures 3c and 3d and Figures S25c, S25d in Supporting Information S1). Despite this, we can visually identify regions of coherency within the maps, and correspondence with AS, particularly for the 660 (Figure 3d, Figure S25d in Supporting Information S1). There is a predominance of deep 660 measurements in locations associated with high seismic velocity in tomography models (French & Romanowicz, 2014; Ritsema et al., 2011), and shallower signals extending beneath the low velocity Pacific Ocean.

4. Thermochemical Modeling and Inversion

We next computed full synthetic seismic waveforms for various mantle mineral models, following the methodology of Waszek et al. (2021), with the thermodynamic algorithm from Connolly (2005), mineral database of Stixrude and Lithgow-Bertelloni (2011), and compositions based on Baker and Stolper (1994). Our models comprise mechanical mixtures of basalt (Gale et al., 2013) and harzburgite (Afonso et al., 2008) in proportions from 0%–100%, in jumps of 10%, and mantle geotherms from 1,000–2,400 K in jumps of 100 K. From these, we generate synthetic seismograms using a reflectivity algorithm (Fuchs & Müller, 1971).

We generate noise-free 1D synthetic seismograms of ScSScS and its precursors for the full range of thermochemical models, using a synthetic dip-slip event at 450 km depth, and synthetic receivers from 0.5–60° epicentral distance every 0.5°. The resultant seismograms are stacked into vespagrams using a reference distance of 30.25°. We extract amplitudes along the theoretical time-slowness line for ScSScS precursors, as predicted by each model, to obtain idealized responses to temperature and composition.

Our modeling reveals a thermal control for the depths of the 410 and 660 signals, and a compositional dependence for the amplitudes (Figures 4a and 4b and Figures S26, S27 in Supporting Information S1). For constant basalt fraction, the 410 depth decreases as temperature increases, and the 660 depth slightly increases (Figure S27a in Supporting Information S1). Thus, MTZ separation provides a thermometer, as for other seismic phases (Munch et al., 2020; Ritsema et al., 2009; Waszek et al., 2021). For constant temperature, both 410 and 660 amplitudes decrease with increasing basalt (Figures S28b and S28c in Supporting Information S1). The limit of visibility is 60–70% basalt in noise-free synthetics (Figures S26 and S27 in Supporting Information S1).

The 1D synthetics provide theoretical 410 and 660 depth and amplitude for each model (Figure S28 in Supporting Information S1), which we interpolate linearly in steps of temperature $T = 10$ K and basalt fraction $f = 0.01$. We invert our measurements (MTZ thickness, discontinuity depths, corrected relative amplitudes) to obtain thermochemical maps for the MTZ, following the methodology of Tauzin et al. (2022) (Figures 4c and 4d and Figures S29–S31 in Supporting Information S1). We restrict our model parameters to basalt fractions of 70% or lower, per the predicted limit of signal visibility, and temperatures of 1,200–1,900 K, corresponding to realistic upper mantle temperatures. We use a uniform prior distribution for the parameters, and incorporate measurement errors for uncertainties on model parameters (Tauzin et al., 2022). We previously estimated experimental errors for thermochemical models to cause approximately ± 5 km of variation in MTZ thickness, which falls within our measurement errors.

The thermal maps are considerably more robust than composition, which has greater uncertainty resulting from larger errors on amplitudes. Furthermore, amplitudes will typically be reduced as a result of incoherent stacking, and thus favor basalt-enriched compositions, however our models have lower basalt content than global

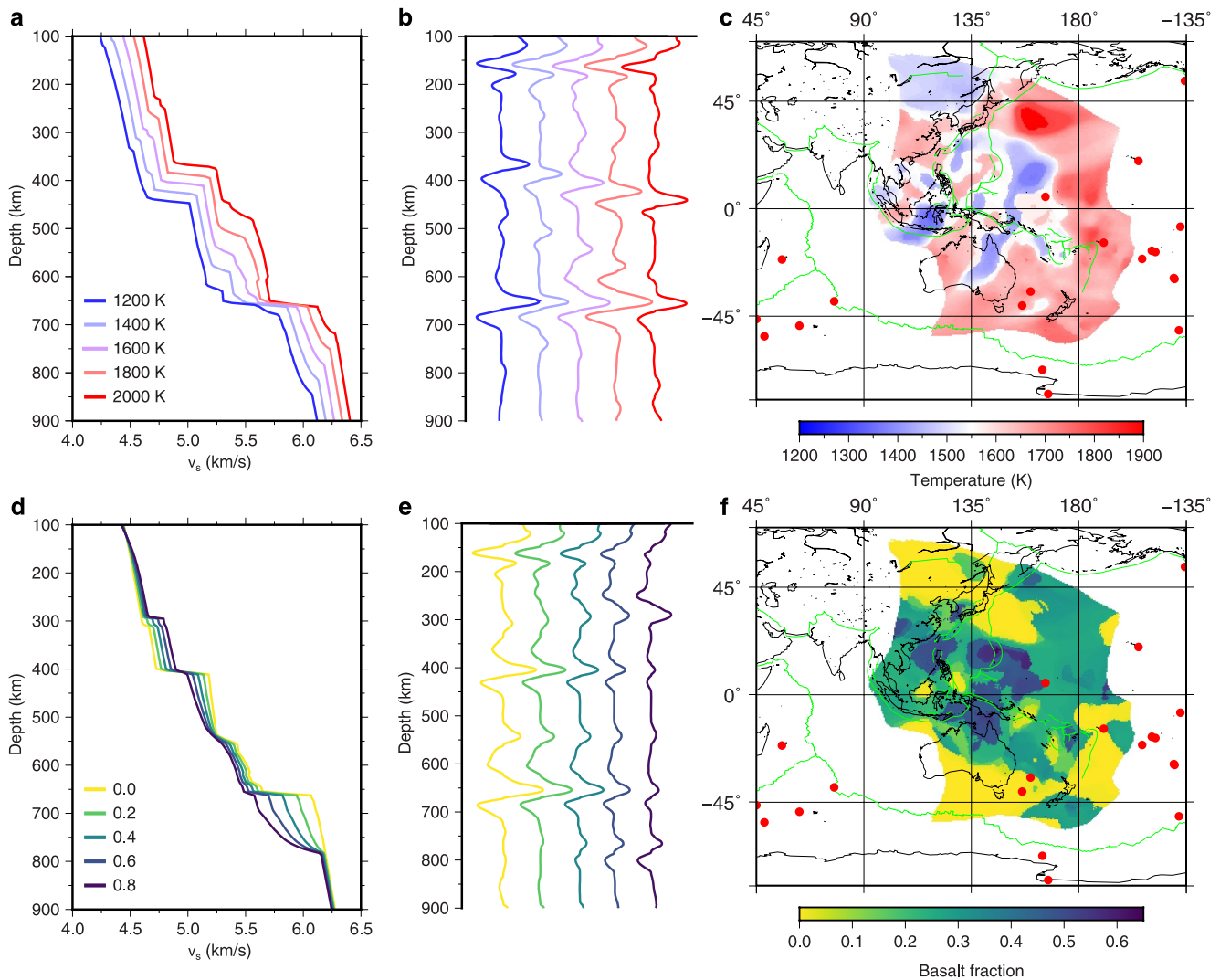


Figure 4. Mineral physics modeling for ScSScS and thermochemical inversion for autopicked data. (a) Velocity profiles calculated for a mechanical mixture of 20% basalt 80% harzburgite, for a range of temperatures. (b) Synthetic waveforms for varying temperature. (c) Temperature field. (d) Velocity profiles calculated for a potential temperature of 1,600 K, for a range of mechanical mixtures of basalt and harzburgite with basalt fractions from 0 to 80%. (e) Synthetic waveforms for varying basalt fraction. (f) Compositional field.

predictions (Table S4 in Supporting Information S1). Thus, we prioritize temperature for comparison to geodynamics, and examine patterns of basalt content rather than absolute values.

Our thermochemical inversions favor low temperatures in regions of thick MTZ (Figure 4c), with correlation to high seismic velocity in tomography models (Figure S24 in Supporting Information S1). Basalt fraction is predicted to be higher within the major subduction region beneath the central western Pacific (Figure 4d). The models show some correlation between low temperature and high basalt fraction, but not everywhere, highlighting the independence of the two parameters. Comparing to measurements from SS data, our models have lower temperatures (~ 60 K) than the global average, but similar to that obtained for the same locations (Table S4 in Supporting Information S1).

5. Discussion

Compilation and processing of seismic data sets represents a significant time investment. Previously, we demonstrated that Autopicker trained on SS can identify its precursors (Garcia et al., 2021a), and we show here that the model can identify ScSScS and precursors at similar periods. For retention criterion of pick quality 60% or

greater, Autopicker retains approximately 2.5 times as many seismograms as handpicking. Example seismograms reveals the consistent shape of automatically picked waveforms (Figures S2–S4 in Supporting Information S1). The higher number of autopicked data reflects the consistent, non-subjective identification capability of Autopicker, emphasized by its capacity to extract precursors in individual data.

The automatically picked data has only slightly improved geographical coverage versus handpicked, due to our restrictions on locations for events, stations, and bounce points. However, it has considerably greater bounce point density (Figures 1d and 1e). The maps of MTZ thickness from the two data sets display moderate positive correlation ($p = 0.66$), with similar correlations between other measurements (Table S2 in Supporting Information S1). The maps show good agreement to those obtained from SS precursors as well as tomography (Figure S24 in Supporting Information S1). The AS maps provide an improvement in spatial coverage and resolution over fixed bins, as well as a consistent and automated approach with statistical outputs.

Clustering analysis applied to ScSScS autopicks of precursors in individual data identifies and extracts statistically distinct signals associated with major mantle discontinuities. This represents an entirely new type of seismic data for studying the upper mantle discontinuities, for example, within the use of high-resolution tomographical inversions. Our automated pipeline therefore has wide-ranging potential for application to other seismic phases, for identification, compilation, stacking, and clustering to extract high quality measurements of discontinuity properties.

We obtain new topography maps of the MTZ beneath the western circum-Pacific region. This area displays highly complex slab dynamics (Chang et al., 2016; Fukao & Obayashi, 2013), but has poor coverage in SS and PP precursors (Deuss, 2009; Schmerr & Garnero, 2007; Shearer & Flanagan, 1999; Waszek et al., 2021), and mostly cannot be mapped by receiver functions. The complementary ScSScS geometries provide resolution on lateral scales on the order of 500 km, and highlight the need for integration of multiple seismic data sets for deep Earth studies (Waszek, 2024).

Our thermochemical model indicates complex patterns on small spatial lengthscales. Temperature signifies recent subduction, due to thermal equilibration, and composition tracks longer circulation processes. Examining inversions for discontinuities separately (Figures S30 and S31 in Supporting Information S1), cold regions at the 410 are smaller and lower temperature than those at the 660, which appear more diffuse. This corresponds to slabs traversing the 410 unimpeded, with some becoming stagnant at the 660. A similar pattern is mapped by GAP-P4 (Fukao & Obayashi, 2013), whereby fast regions are smaller and higher velocity at the 410 than at the 660 (Figure S32 in Supporting Information S1), and the diffuse cold regions at the 660 display no correlation to deep focus earthquakes (Figure S33 in Supporting Information S1), consistent with stagnation. Conversely, the deep seismicity appears clusters near to the edges of the cold regions at the 410 (Figures S30 and S31 in Supporting Information S1), in line with active subduction here.

High temperature regions in our model are generally hotter at the 660 than the 410, suggesting widespread ponding of plumes beneath the MTZ (Waszek et al., 2021). The upwelling plumes here exhibit diverse interactions with downgoing slabs, which our results corroborate. Samoa is located in a region of high temperature and significant seismicity, indicating its significant impact on the dynamics of the Tonga-Kermadec subduction system (Chang et al., 2016). Caroline is situated at the edge of a diffuse cold region marking the stagnant Pacific slab, which acts to impede upward transport of plume material (Obayashi et al., 2021).

Noting larger uncertainties on amplitudes reflected in disagreement between data sets, our models suggest basalt enrichment at the 660 which extends beyond active subduction zones, supporting persistent basalt accumulation (Tauzin et al., 2022). Other compositional variations should also be considered, particularly the impact of water (Karato, 2011), which reduces seismic wavespeed and according to laboratory data should also increase MTZ separation (Houser, 2016; Ohtani et al., 2004; Thio et al., 2016). Our observations are mostly inconsistent with the signature of water, excluding some regions in the central western Pacific (Figure 2 and Figures S24, S31 in Supporting Information S1). Differences in lengthscales preclude further analysis, and other upper mantle discontinuities should be included for in-depth investigations.

6. Conclusions

This study demonstrates the potential of various automated techniques for compilation, processing, and modeling of seismic phases sensitive to MTZ discontinuities, some of which are unable to be identified using traditional

methods. Our findings highlight the need for integration of multiple types of data sets and approaches for improving global resolution. As proof-of-concept, we apply the methods to ScSScS data beneath the western Pacific, which provide good illumination of these diverse subduction settings poorly covered by other data. Observations reveal variable topography, and good correspondence to seismic tomography models.

Seismic measurements are integrated with mineral physics modeling calculations to obtain regional scale thermochemical maps for the upper mantle. Temperature near to active subduction regions tracks the recent route of slabs through the MTZ, indicating direct passage through the 410, but stagnation at the 660. Similarly, temperatures outside of subduction zones are higher at the 660, suggesting ponding of upwelling beneath the MTZ and complex dynamics between plumes and slabs. Basalt enrichment at the 660 implies longer term accumulation of slab material within the MTZ.

Our results suggest that detailed maps of the upper mantle discontinuities can be used to obtain high-resolution images of mantle convection patterns, with implications for mixing processes and circulation history.

Data Availability Statement

Original waveform data are available from the IRIS Data Management Center (NSF Grant EAR-1063471). Full data sets, lists of event and station information, measurements of the 410 and 660 km discontinuities, and the thermochemical models, are available via Waszek et al. (2024). The Autopicker code is available via Garcia et al. (2021b). The adaptive stacking and mineral physics modeling codes, and mineral physics databases are available at Tauzin et al. (2021), Tauzin and Waszek (2021).

References

- Afonso, J., Fernandez, M., Ranalli, G., Griffin, W., & Connolly, J. (2008). Integrated geophysical-petrological modelling of the lithosphere and sublithospheric upper mantle: Methodology and applications. *Geochemistry, Geophysics, Geosystems*, 9(5), Q05008. <https://doi.org/10.1029/2007GC001834>
- Baker, M., & Stolper, E. (1994). Determining the composition of high-pressure mantle melts using diamond aggregates. *Geochimica et Cosmochimica Acta*, 58(13), 2811–2827. [https://doi.org/10.1016/0016-7037\(94\)90116-3](https://doi.org/10.1016/0016-7037(94)90116-3)
- Bassin, C., Laske, G., & Masters, G. (2000). The current limits of resolution for surface wave tomography in North America. *EOS, Transactions AGU*, 81, F897.
- Campello, R. J. G. B., Moulavi, D., & Sander, J. (2013). Density-based clustering based on hierarchical density estimates. In J. Pei, V. S. Tseng, L. Cao, H. Motoda, & G. Xu (Eds.), *Advances in knowledge Discovery and data mining* (pp. 160–172). Springer. https://doi.org/10.1007/978-3-642-37456-2_14
- Chang, S.-J., Ferreira, A., & Faccenda, M. (2016). Upper- and mid-mantle interaction between the Samoan plume and the Tonga–Kermadec slabs. *Nature Communications*, 7(10799), 10799. <https://doi.org/10.1038/ncomms10799>
- Christensen, U. (1995). Effects of phase transitions on mantle convection. *Annual Review of Earth and Planetary Sciences*, 23(1), 65–87. <https://doi.org/10.1146/annurev.earth.23.1.65>
- Connolly, J. (2005). Computation of phase equilibria by linear programming: A tool for geodynamic modeling and its application to subduction zone decarbonation. *Earth and Planetary Science Letters*, 236(1–2), 524–541. <https://doi.org/10.1016/j.epsl.2005.04.033>
- Conrad, C., Bilek, S., & Lithgow-Bertelloni, C. (2004). Great earthquakes and slab pull: Interaction between seismic coupling and plate–slab coupling. *Earth and Planetary Science Letters*, 218(1–2), 109–122. [https://doi.org/10.1016/S0012-821X\(03\)00643-5](https://doi.org/10.1016/S0012-821X(03)00643-5)
- Courtier, A., & Revenaugh, J. (2007). Deep upper-mantle melting beneath the Tasman and Coral Seas detected with multiple ScS reverberations. *Earth and Planetary Science Letters*, 259(1), 66–76. <https://doi.org/10.1016/j.epsl.2007.04.027>
- Crotwell, H., Owens, T., & Ritsema, J. (1999). The TauP Toolkit: Flexible seismic travel-time and raypath utilities. *Seismological Research Letters*, 70(2), 154–160. <https://doi.org/10.1785/gssrl.70.2.154>
- Deuss, A. (2009). Global observations of mantle discontinuities using SS and PP precursors. *Surveys in Geophysics*, 30(4–5), 301–326. <https://doi.org/10.1007/s10712-009-9078-y>
- Dziewoński, A., & Anderson, D. (1981). Preliminary reference Earth model. *Physics of the Earth and Planetary Interiors*, 25(4), 297–356. [https://doi.org/10.1016/0031-9201\(81\)90046-7](https://doi.org/10.1016/0031-9201(81)90046-7)
- Ekström, G., Nettles, M., & Dziewoński, A. (2012). The global CMT project 2004–2010: Centroid-moment tensors for 13,017 earthquakes. *Physics of the Earth and Planetary Interiors*, 200–201, 1–9. <https://doi.org/10.1016/j.pepi.2012.04.002>
- French, S., & Romanowicz, B. (2014). Whole-mantle radially anisotropic shear-velocity structure from spectral-element waveform tomography. *Geophysical Journal International*, 199(3), 1303–1327. <https://doi.org/10.1093/gji/ggu334>
- Fuchs, K., & Müller, G. (1971). Computation of synthetic seismograms with the reflectivity method and comparison with observations. *Geophysical Journal International*, 23(4), 417–433. <https://doi.org/10.1111/j.1365-246x.1971.tb01834.x>
- Fukao, Y., & Obayashi, M. (2013). Subducted slabs stagnant above, penetrating through, and trapped below the 660 km discontinuity. *Journal of Geophysical Research: Solid Earth*, 118(11), 5920–5938. <https://doi.org/10.1002/2013JB010466>
- Gale, A., Dalton, C., Langmuir, C., Su, Y., & Schilling, J. (2013). The mean composition of ocean ridge basalts. *Geochemistry, Geophysics, Geosystems*, 14(3), 489–518. <https://doi.org/10.1029/2012GC004334>
- Garcia, J., Waszek, L., Tauzin, B., & Schmerr, N. (2021a). Automated identification of seismic wave arrivals using Convolutional Neural Networks. *Geophysical Research Letters*, 48(18), e2020GL091658. <https://doi.org/10.1029/2020GL091658>
- Garcia, J., Waszek, L., Tauzin, B., & Schmerr, N. (2021b). Automatic identification of mantle seismic phases using a Convolutional Neural Network. <https://doi.org/10.5281/zenodo.4827004>

Acknowledgments

We are grateful to Jeroen Ritsema and an anonymous reviewer for their thoughtful comments to help improve the paper. We acknowledge support from a Discovery Early Career Research Award (project number DE170100329), funded by the Australian Government (L.W.), the National Science Foundation (NSF) under Grant EAR-1661985 and EAR-1853662 (L.W. and R.A.), and the European Union's Horizon 2020 Research and Innovation programme under the Marie Skłodowska-Curie grant agreement 793824 (B.T.). All seismic data were downloaded through the EarthScope Consortium Wilber 3 system (<https://ds.iris.edu/wilber3/>). Figures were plotted using Generic Mapping Tools (Wessel et al., 2019) and SubMachine (Hosseini et al., 2018). Open access publishing facilitated by James Cook University, as part of the Wiley - James Cook University agreement via the Council of Australian University Librarians.

- Goldstein, P., Dodge, D., Firpo, M., & Minner, L. (2003). SAC2000: Signal processing and analysis tools for seismologists and engineers. In *The IASPEI international handbook of earthquake and engineering seismology* (pp. 1613–1614).
- Hahsler, M., Piekenbrock, M., & Doran, D. (2019). dbscan: Fast density-based clustering with R. *Journal of Statistical Software*, *91*(1), 1–30. <https://doi.org/10.18637/jss.v091.i01>
- Haugland, S., Ritsema, J., Sun, D., Trampert, J., & Koroni, M. (2019). Common reflection point mapping of the mantle transition zone using recorded and 3-D synthetic ScS reverberations. *Geophysical Journal International*, *220*(1), 724–736. <https://doi.org/10.1093/gji/ggz467>
- Hirose, K. (2002). Phase transitions in pyrolytic mantle around 670-km depth: Implications for upwelling of plumes from the lower mantle. *Journal of Geophysical Research*, *107*, 2078. <https://doi.org/10.1029/2001jb000597>
- Hosseini, K., Matthews, K., Sigloch, K., Shephard, G., Domeier, M., & Tsekhmistrenko, M. (2018). Submachine: Web-based tools for exploring seismic tomography and other models of Earth's deep interior. *Geochemistry, Geophysics, Geosystems*, *19*(5), 1464–1483. <https://doi.org/10.1029/2018GC007431>
- Houser, C. (2016). Global seismic data reveal little water in the mantle transition zone. *Earth and Planetary Science Letters*, *448*, 94–101. <https://doi.org/10.1016/j.epsl.2016.04.018>
- Houser, C., & Williams, Q. (2009). Reconciling pacific 410 and 660 km discontinuity topography, transition zone shear velocity patterns, and mantle phase transitions. *Earth and Planetary Science Letters*, *296*(3–4), 255–266. <https://doi.org/10.1016/j.epsl.2010.05.006>
- Huang, Q., Schmerr, N., Waszek, L., & Beghein, C. (2019). Constraints on seismic anisotropy in the mantle transition zone from long-period SS precursors. *Journal of Geophysical Research*, *124*(7), 6779–6800. <https://doi.org/10.1029/2019JC017307>
- Karato, S. (2011). Water distribution across the mantle transition zone and its implications for global material circulation. *Earth and Planetary Science Letters*, *301*(3–4), 413–423. <https://doi.org/10.1016/j.epsl.2010.11.038>
- Lawrence, J., & Shearer, P. (2006). A global study of transition zone thickness using receiver functions. *Journal of Geophysical Research*, *111*(B6), B06307. <https://doi.org/10.1029/2005JB003973>
- Munch, F., Khan, A., Tauzin, B., van Driel, M., & Giardini, D. (2020). Seismological evidence for thermochemical heterogeneity in Earth's continental mantle. *Earth and Planetary Science Letters*, *539*, 116240. <https://doi.org/10.1016/j.epsl.2020.116240>
- Obayashi, M., Yoshimitsu, J., Suetsugu, D., Shiobara, H., Sugioka, H., Ito, A., et al. (2021). Interrelation of the stagnant slab, Ontong Java Plateau, and intraplate volcanism as inferred from seismic tomography. *Scientific Reports*, *11*(1), 20966. <https://doi.org/10.1038/s41598-021-99833-5>
- Ohtani, E., Litasov, K., Hosoya, T., Kubo, T., & Kondo, T. (2004). Water transport into the deep mantle and formation of a hydrous transition zone. *Physics of the Earth and Planetary Interiors*, *143–144*, 255–269. <https://doi.org/10.1016/j.pepi.2003.09.015>
- Pugh, S., Jenkins, J., Boyce, A., & Cottaar, S. (2021). Global receiver function observations of the X-discontinuity reveal recycled basalt beneath hotspots. *Earth and Planetary Science Letters*, *561*, 116813. <https://doi.org/10.1016/j.epsl.2021.116813>
- Revenaugh, J., & Jordan, T. (1991). Mantle layering from ScS reverberations: 2. The transition zone. *Journal of Geophysical Research*, *91*, 19673–19780.
- Ritsema, J., Deuss, A., van Heijst, H., & Woodhouse, J. (2011). S40RTS: A degree-40 shear-velocity model for the mantle from new Rayleigh wave dispersion, teleseismic traveltimes and normal-mode splitting function measurements. *Geophysical Journal International*, *184*(3), 1223–1236. <https://doi.org/10.1111/j.1365-246x.2010.04884.x>
- Ritsema, J., Xu, W., Stixrude, L., & Lithgow-Bertelloni, C. (2009). Estimates of the transition zone temperature in a mechanically mixed upper mantle. *Earth and Planetary Science Letters*, *277*(1–2), 244–252. <https://doi.org/10.1016/j.epsl.2008.10.024>
- Schmerr, N., & Garnero, E. (2007). Upper mantle discontinuity topography from thermal and chemical heterogeneity. *Science*, *318*(5830), 623–626. <https://doi.org/10.1126/science.1145962>
- Shearer, P. (1991). Constraints on upper mantle discontinuities from observations of long-period reflected and converted phases. *Journal of Geophysical Research*, *96*(B11), 18147–18182. <https://doi.org/10.1029/91jb01592>
- Shearer, P., & Flanagan, M. (1999). Seismic velocity and density jumps across the 410- and 660- kilometer discontinuities. *Science*, *285*(5433), 1545–1548. <https://doi.org/10.1126/science.285.5433.1545>
- Stixrude, L., & Lithgow-Bertelloni, C. (2011). Thermodynamics of mantle minerals – II. phase equilibria. *Geophysical Journal International*, *184*(3), 1180–1213. <https://doi.org/10.1111/j.1365-246x.2010.04890.x>
- Suetsugu, D., Saita, T., Takenaka, H., & Niu, F. (2004). Thickness of the mantle transition zone beneath the South Pacific as inferred from analyses of ScS reverberated and Ps converted waves. *Physics of the Earth and Planetary Interiors*, *146*(1), 35–46. <https://doi.org/10.1016/j.pepi.2003.06.008>
- Tackley, P., Stevenson, D., Glatzmaier, G., & Schubert, G. (1993). Effects of an endothermic phase transition at 670 km depth in a spherical model of convection in the Earth's mantle. *Nature*, *361*(6414), 699–704. <https://doi.org/10.1038/361699a0>
- Tauzin, B., Debayle, E., & Wittlinger, G. (2008). The mantle transition zone as seen by global Pds phases: No clear evidence for a thin transition zone beneath hotspots. *Journal of Geophysical Research*, *113*(B8), B08309. <https://doi.org/10.1029/2007JB005364>
- Tauzin, B., & Waszek, L. (2021). NoLiMit MATLAB package v1.0. Non-Linear Bayesian partition Modeling of the Earth's Mantle Transition zone. *Proceedings of the National Academy of Sciences*, *119*(48), e2209399119. <https://doi.org/10.5281/zenodo.5512804>
- Tauzin, B., Waszek, L., & Afonso, J. (2021). Catalog of synthetic seismic records from mineral physics and travel-time tables from Waszek et al., 2021. *Nature Geoscience*. <https://doi.org/10.5281/zenodo.5512035>
- Tauzin, B., Waszek, L., Ballmer, M., Afonso, J., & Bodin, T. (2022). Basaltic mantle reservoirs from probabilistic inversion of seismic reflection data. *Proceedings of the National Academy of Sciences*, *119*(48), e2209399119. <https://doi.org/10.1073/pnas.2209399119>
- Thio, V., Cobden, L., & Trampert, J. (2016). Seismic signature of a hydrous mantle transition zone. *Physics of the Earth and Planetary Interiors*, *250*, 46–63. <https://doi.org/10.1016/j.pepi.2015.11.005>
- Tian, D., Lv, M., Wei, S., Dorfman, S., & Shearer, P. (2020). Global variations of Earth's 520- and 560-km discontinuities. *Earth and Planetary Science Letters*, *552*, 116600. <https://doi.org/10.1016/j.epsl.2020.116600>
- Vinnik, L. (1977). Detection of waves converted from P to SV in the mantle. *Physics of the Earth and Planetary Interiors*, *15*(1), 39–45. [https://doi.org/10.1016/0031-9201\(77\)90008-5](https://doi.org/10.1016/0031-9201(77)90008-5)
- Wang, X., Li, J., & Chen, Q. (2017). Topography of the 410 km and 660 km discontinuities beneath the Japan Sea and adjacent regions by analysis of multiple-ScS waves. *Journal of Geophysical Research: Solid Earth*, *122*(2), 1264–1283. <https://doi.org/10.1002/2016JB013357>
- Waszek, L. (2024). Seismic methodologies key to unlocking Earth's lowermost mantle. *Nature Geoscience*, *17*(4), 272–274. <https://doi.org/10.1038/z41561-024-01416-2>
- Waszek, L., Anandanwansa, R., Sexton, J., & Tauzin, B. (2024). Datasets associated with “Thermochemistry of the mantle transition zone beneath the western Pacific” [Dataset]. *Zenodo*. <https://doi.org/10.5281/zenodo.12521545>
- Waszek, L., Schmerr, N., & Ballmer, M. (2018). Global observations of reflectors in the mid-mantle with implications for mantle structure and dynamics. *Nature Communications*, *9*(385), 385. <https://doi.org/10.1038/s41467-017-02709-4>

- Waszek, L., Tauzin, B., Schmerr, N., Ballmer, M., & Afonso, J. (2021). A poorly mixed mantle transition zone and its thermal state inferred from seismic waves. *Nature Geoscience*, *14*(12), 949–955. <https://doi.org/10.1038/s41561-021-00850-w>
- Wessel, P., Luis, J., Uieda, L., Scharroo, R., Wobbe, F., Smith, W., & Tian, D. (2019). The Generic Mapping Tools version 6. *Geochemistry, Geophysics, Geosystems*, *20*(11), 5556–5564. <https://doi.org/10.1029/2019GC008515>
- Yu, C., Goes, S., Day, E., & van der Hilst, R. (2023). Seismic evidence for global basalt accumulation in the mantle transition zone. *Science Advances*, *9*(22), eadg0095. <https://doi.org/10.1126/sciadv.adg0095>